Competition Between Acoustic Radiation Forces and Hydrodynamic Drag in Short-Pulsed-Ultrasound-Driven Microbubble Cluster Dynamics in Microfluidic Channel

Authors

Yi Xu[a,b,#], Siyu Luo[b,c,#], Yujie Wang[b], Liying Wang[a,*], Yuzhe Fan[d,*], Fenfang Li[b,*]

Affiliations

[a]School of Basic Medical Sciences, Beihua University, Jilin City, China
[b]Institute of Molecular Physiology, Shenzhen Bay Laboratory, Shenzhen, China
[c]School of Biology and Biological Engineering, South China University of Technology, Guangzhou 510006, China
[d]Institute of Physics, Otto-von-Guericke University Magdeburg
[#] These authors contributed equally
*Corresponding authors: bhwly@beihua.edu.cn, fenfang.li@szbl.ac.cn, yuzhe.fan@ovgu.de

Abstract

Microbubble dynamics under short-pulse ultrasound in flowing environments are governed by the interplay between acoustic radiation forces and hydrodynamic drag, yet their coupled effects remain insufficiently understood. Here, we investigate microbubble cloud behaviour in a vessel-mimicking microfluidic channel under short-pulse ultrasound (1.125 MHz) and controlled laminar flow (37.5–150 µL/min). High-speed visualization reveals two distinct regimes: an actively interacting regime characterized by clustering and coalescence, and a ‘frozen’ regime in which microbubbles exhibit minimal displacement despite continued ultrasound excitation. A theoretical model incorporating lift force, Bjerknes forces, wall-induced hydrodynamic interaction, and hydrodynamic drag with wall correction captures the transition between actively moving and frozen states, confirming that both a low flow rate and short-pulse ultrasound sequences promote the development of ‘frozen’ bubble nearby the wall, and demonstrating that microbubble cloud dynamics under short-pulse excitation is determined by a dynamic competition between acoustic radiation forces and near-wall hydrodynamic drag, with flow rate and pulse duration acting as coupled control parameters.

Keywords

Acoustic cavitation; Vessel-mimicking microchannels; Flow velocity; Short pulse ultrasound; Duty cycle

1. Introduction

Microbubble-assisted non-thermal focused ultrasound therapy has attracted increasing attention in recent years because of its unique advantages in brain drug delivery, tissue ablation, and immune modulation [1]. In this approach, coated microbubbles, also known as ultrasound contrast agents (UCAs) [2, 3], are injected into the body as exogenous cavitation nuclei [4]. Under ultrasound excitation, these microbubbles can undergo stable oscillations accompanied by cyclic jet formation [5], or they can experience inertial cavitation, in which excessive expansion during rarefaction is followed by violent collapse. Non-inertial cavitation is generally preferred for producing subtle and transient biological effects, whereas inertial cavitation can be exploited to induce localized tissue damage [6-9].

Although single-microbubble dynamics and their interactions with surrounding tissues or phantoms have been extensively investigated, exogenous microbubbles exist in vivo as bubble clouds rather than isolated entities. Within such clouds, complex bubble–bubble interactions give rise to large secondary acoustic emissions [10-13], driving microbubble migration [14-16], clustering [17, 18], and coalescence [19]. In particular, acoustic radiation forces generated by the external ultrasound field or by oscillating neighboring bubbles can induce pronounced clustering of microbubbles [20] and enhance UCA attachment to target surfaces [21]. These processes suggest that ultrasound can strongly influence the spatiotemporal structure of bubble clouds and thereby modulate therapeutic outcomes.

In most preclinical and clinical studies, long-pulse (LP) ultrasound sequences are employed, as robust therapeutic effects can be achieved by prolonging acoustic exposure to open the endothelial barrier [22]. However, these approaches are also associated with adverse bioeffects, including erythrocyte extravasation [23], edema [24], and neuroinflammation [25]. In contrast, emerging short-pulse (SP) ultrasound protocols, characterized by brief and repetitive bursts, deliver substantially less total energy and have shown promise for achieving more uniform and reversible barrier opening with minimal tissue damage [26-29]. Under short-pulse operation, appropriate adjustment of the duty cycle can balance microbubble replenishment with acoustic energy input, which may be achieved through reducing fragmentation, clustering and coalescence [30, 31]. However, A critical gap remains in our understanding of the intricate interplay of cavitation dynamics under varying physiologically relevant flow conditions, both within a single short pulse and across successive short pulses. Only a few studies have employed high-speed microscopy to resolve microbubble dynamics under short pulse sequences [31]. Yet there is a lack of spatiotemporal resolution to capture both individual bubble and bubble cloud behavior under short-pulse ultrasound excitation. In addition, in physiological environments, hemodynamic flow conditions vary widely and directly modulate bubble trajectories, spatial distribution, and residence time [32]. Clinically, hemodynamic characteristics differ substantially across pathological tissues [33]. For example, tumor vasculature exhibits reduced flow velocities (5–15 mm/s) compared with normal microvascular flow due to structural abnormalities and elevated vascular resistance [33, 34], while ischemic regions exhibit even slower flow [35]. Such hemodynamic heterogeneity strongly influences bubble–flow and bubble–cell interactions [36-39]. Nevertheless, the explicit relationship between ultrasound, particularly short-pulse sequences, and microbubble dynamics under varying flow conditions remains poorly understood [32, 40-42].

In this work, we employ an integrated microfluidic–acoustic platform to investigate the coupled effects of flow velocity and ultrasound duty cycle on microbubble dynamics under short-pulse excitation. Microfluidic systems provide a well-controlled experimental framework for reconstructing vascular-scale environments and precisely regulating flow velocity and shear stress [43-46], while enabling high-resolution visualization of bubble dynamics [47-50]. Using high-speed imaging and quantitative analysis, we systematically characterize individual bubble and bubble cloud behavior across a range of flow rates and duty cycles. Our results reveal competition between acoustic radiation forces and hydrodynamic drag during microbubble clustering and coalescence and demonstrate that flow velocity can determine the microbubble cloud dynamics near the wall.

2. Materials and methods

2.1 Vessel-mimicking microchannel fabrication

Each microfluidic channel used in this study is 200 µm in width, 100 µm in height, and 17000 µm in length. The PDMS wall on top of the channels is made 3mm thick to align the ultrasound beam focus at the channel in the Z direction. Marker patterns were integrated in the design of microchannels, allowing precise X-Y positioning and focus of the ring ultrasound transducer to the channels. The microchannels mimicking vascular structures were designed using SU-8 master mold produced through standard soft lithography techniques. A 10:1 mixture of polydimethylsiloxane (PDMS, Sylgard 184 Silicone Elastomer Kit, Dow Corning) was poured onto the mold, cured at 60 °C for 4 h, and subsequently bonded to #1 cover glass slides (25×50 mm^2) immediately after a 50 s plasma treatment (Diener, Zepto one).

2.2 Preparation and characterization of microbubbles

Microbubbles composed of a lipid shell and filled with perfluoropropane gas were generated according to previously described methods [51]. The lipid formulation consisted of 1,2-distearoyl-sn-glycero-3-phosphocholine (DSPC) and N-(carbonyl-methoxypolyethylene glycol-2000)-1,2-distearoyl-sn-glycero-3-phosphoethanolamine (DSPE-PEG2000) (Lipoid, Ludwigshafen, Germany) in a 9:1 molar ratio. After the synthesis process, the microbubbles were diluted with Isoton II solution, and their concentration and size distribution were measured using a Coulter Counter Multisizer IV (Beckman Coulter Inc., USA). Their morphology was then examined under a microscope (Zeiss, Axio Observer 7). The morphology, size distribution and stability of the home-made microbubbles is similar to our previous studies [52, 53].

2.3 Setup for recording bubble dynamics in microchannels under ultrasound exposure and varying flow conditions

For the bubble dynamics experiments, previously prepared polydisperse microbubbles were diluted 1:20 (v/v) in 1× Dulbecco's phosphate-buffered saline (DPBS) and introduced into the microchannels at flow rates of 37.5, 75 and 150 µL/min using a syringe pump (KDS, R462) mounted on an inverted microscope (Zeiss, Axio Observer 7), as shown in Fig. 1A. Sonication was performed using a custom-built ring-shaped ultrasound transducer operating at 1.125 MHz and driven by a 50-dB power amplifier (2100L, Electronics & Innovation, USA). The transducer was aligned on top of the PDMS chip with designed markers using high-vacuum grease (Dow Corning) as coupling gel. The driving ultrasound signals were generated by two function generators (DG972, RIGOL, China). A short-pulse ultrasound sequence was applied (Fig. 1A) with a peak rarefactional pressure of 0.35 MPa, a pulse repetition frequency of 1 kHz, and pulse lengths ranging from 50 to 100 µs. Bubble motion was imaged under a 63× objective (LD PN 63×/0.75 Corr) using a high-speed camera (Photron, Nova S12) that was synchronized to each ultrasound pulses. The camera operated at 40,000 frames per second with an exposure time of 0.66 µs.

2.4 Qualification and Statistical analysis

High-speed videos of bubble dynamics were imported into MATLAB (The MathWorks, Natick, MA, USA; academic license) for quantitative analysis of microbubble number and motion. The recorded images were first preprocessed using the ‘imflatfield’ function to correct for nonuniform background illumination, followed by median filtering function ‘medfilt2’ to suppress high-frequency noise. Subsequently, images were binarized using the adaptive thresholding function ‘adaptthresh’. Microbubble number and centroid positions were extracted from the binary images using the ‘regionprops’ function.

For microbubble tracking, a nearest-neighbor approach was employed. The position of each bubble in the current frame was matched to the closest bubble in the subsequent frame based on the minimum Euclidean distance criterion. A match was accepted when the minimum-distance condition was satisfied [54].

Significant differences were determined by un-paired Student t-test for comparison between two groups.

3. Results

3.1. The influence of ultrasound and laminar flow rate on bubble dynamics nearby the PDMS surface

In this study, we focus on microbubble cluster dynamics near the upper PDMS wall (Fig. 1A). As shown in Fig. 1B (left), the freshly synthesized microbubbles exhibit a polydisperse size distribution, oscillate under ultrasound excitation, and move downstream with the laminar flow parallel to the wall. When ultrasound is applied, bubbles oscillate strongly and exhibit a tendency to migrate toward one another, leading to clustering. Microbubbles located in the central region of the image (within the small red dashed box and original position marked in yellow) coalesce, while surrounding bubbles migrate toward this region (original position labeled by red dots, Fig. 1B, right top). Once the ultrasound is turned off, the microbubbles resume downstream motion with the background flow at velocities much lower than those observed during ultrasound excitation (Fig. 1B, right bottom).

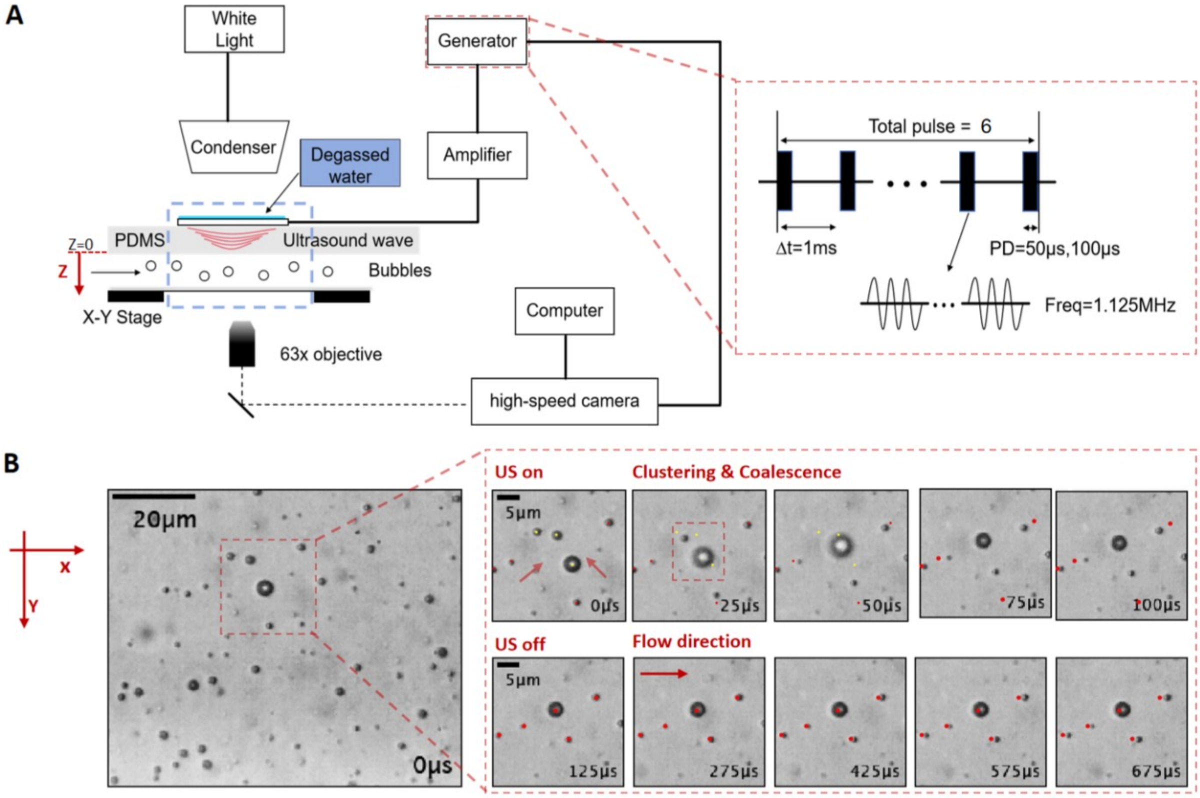

Figure 1. Experimental setup and design. (A) Experimental setup and schematic of the short-pulse ultrasound sequence used in the experiments. (B) High-speed snapshots of bubble dynamics under ultrasound excitation and fluid flow (flow rate: 37.5 μL/min; pulse length: 50 μs). Yellow dots indicate the initial positions of bubbles that subsequently coalesced, whereas red dots indicate the initial positions of bubbles that did not coalesce. Bubbles cluster and coalesce during ultrasound excitation and move downstream with the flow once the ultrasound is turned off.

Figure 2 demonstrates that both flow rate and ultrasound pulse length strongly influence bubble dynamics. In Fig. 2A (flow rate 37.5 μL/min; pulse length 50 μs), bubbles exhibit pronounced motion during ultrasound exposure; however, a “frozen” region is observed in which microbubbles display minimal displacement. A similar spatial heterogeneity is observed for a longer pulse length (Fig. 2B; flow rate 37.5 μL/min; pulse length 100 μs). The longer pulse duration allows more time for in-phase oscillating microbubbles to attract each other, leading to an increased number of coalescence events in the actively moving region (Fig. 2B, red dashed box). In contrast, at a higher flow rate (Fig. 2C; 150 μL/min; pulse length 50 μs), most bubbles respond actively to ultrasound excitation. Under this condition, smaller microbubbles tend to coalesce locally in multiple regions, resulting in the formation of several larger bubbles distributed across the channel.

To quantify these observations, we analyzed the normalized bubble number, $N_{norm}(t) = (N(t) - N_0)/N_0$, where N_0 is the average microbubble number during the 200 μs baseline recording before ultrasound, and $N(t)$ is the bubble count in each recorded frame. As shown in Fig. 2D, both increasing pulse length and increasing flow rate result in a larger drop of the normalized bubble number after 1 burst of ultrasound sequence, and a single pulse excitation already produces an approximately 10% change in $N_{norm}(t)$.

We further quantified the average velocity of microbubbles (over the first 50μs during ultrasound excitation) that did not undergo coalescence during the ultrasound excitation (Fig. 3). The results indicate that the mean microbubble velocity at the higher flow rate (150 μL/min) is significantly greater ($p < 0.01$) than that at the lower flow rate (37.5 μL/min). The measurements quantitatively confirm that microbubbles exhibit stronger motion under ultrasound excitation at higher flow rates. However, one must notice that the direction of bubble motion during ultrasound exposure is not aligned with the background flow and appears random. Moreover, the bubble velocities under ultrasound are substantially greater than the laminar flow velocity. Therefore, the increased flow rate does not directly drive the enhanced bubble motion observed during ultrasound excitation.

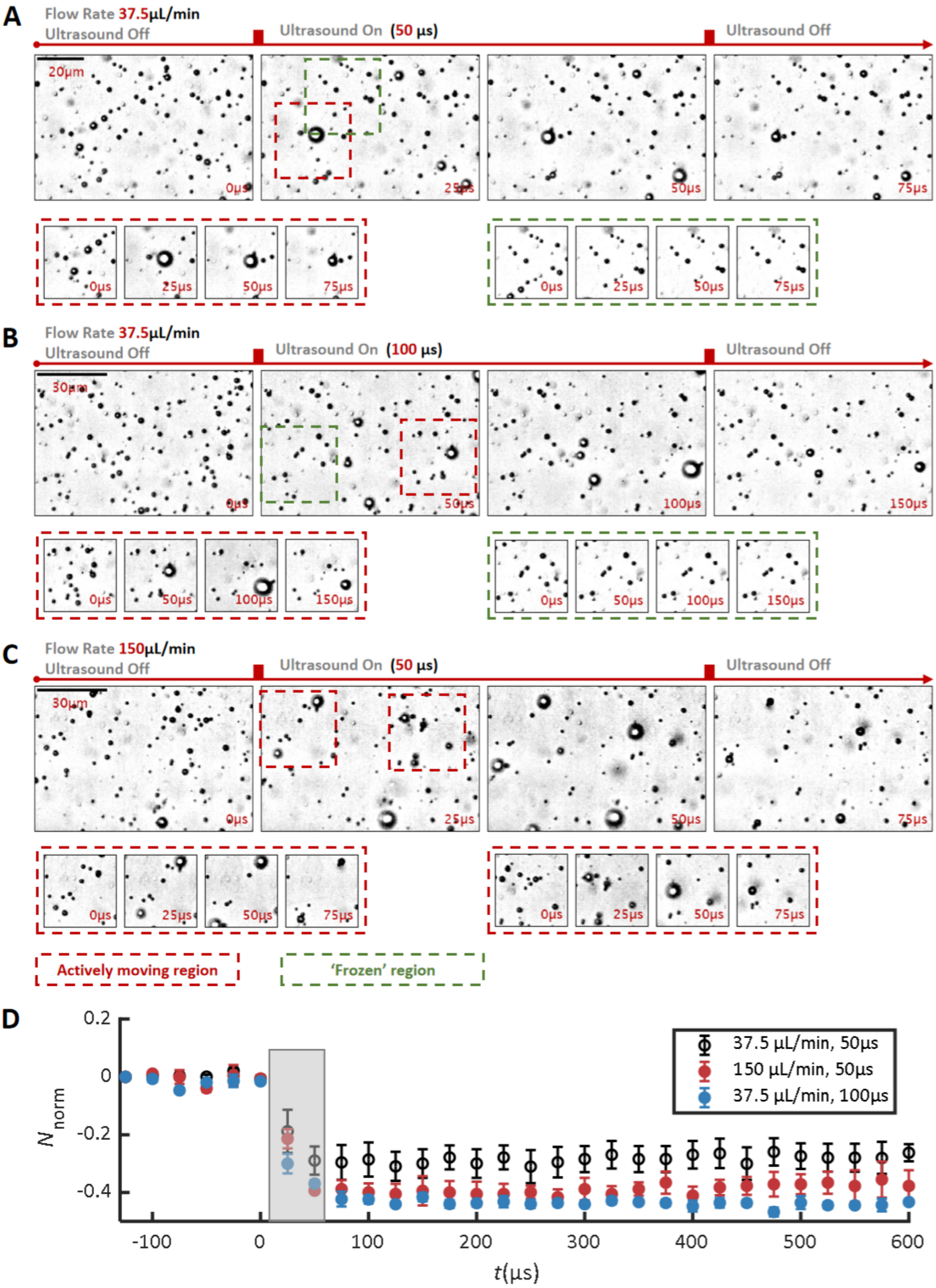

Figure 2. Analysis of bubble motion and bubble dynamics under a single shot-pulse ultrasound sequence. Selected images of bubble motion and dynamics under ultrasound excitation: (A) flow rate 37.5 μL/min, pulse length 50 μs; (B) flow rate 37.5 μL/min, pulse length 100 μs; (C) flow rate 150 μL/min, pulse length 50 μs. The dashed red and dashed green boxes mark the actively moving region and the "frozen" region of microbubbles during ultrasound excitation, respectively. (D) Microbubble number as a function of time under different conditions. Error bars indicate the standard deviation obtained from independent

realizations. Each data represents Mean ±SEM. Three individual videos are analyzed in each of the three conditions.

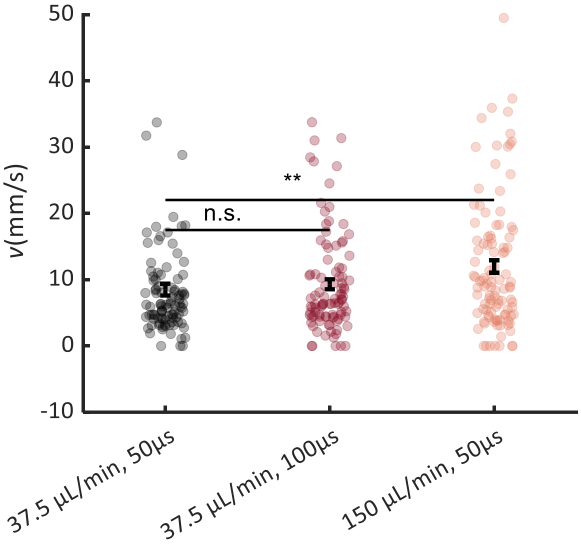

Figure 3. Statistical analysis of microbubble velocity under ultrasound excitation. The average microbubble velocity v during the first 50 μs of ultrasound exposure was quantified. The analysis was restricted to microbubbles that did not undergo coalescence during excitation. Three individual videos are analyzed in each conditions. Unpaired student t test is used for statistical analysis. The number of bubbles analyzed in each group is 98, 106 and 98 from left to right.

3.2. Microbubble dynamics after multiple short-pulse ultrasound

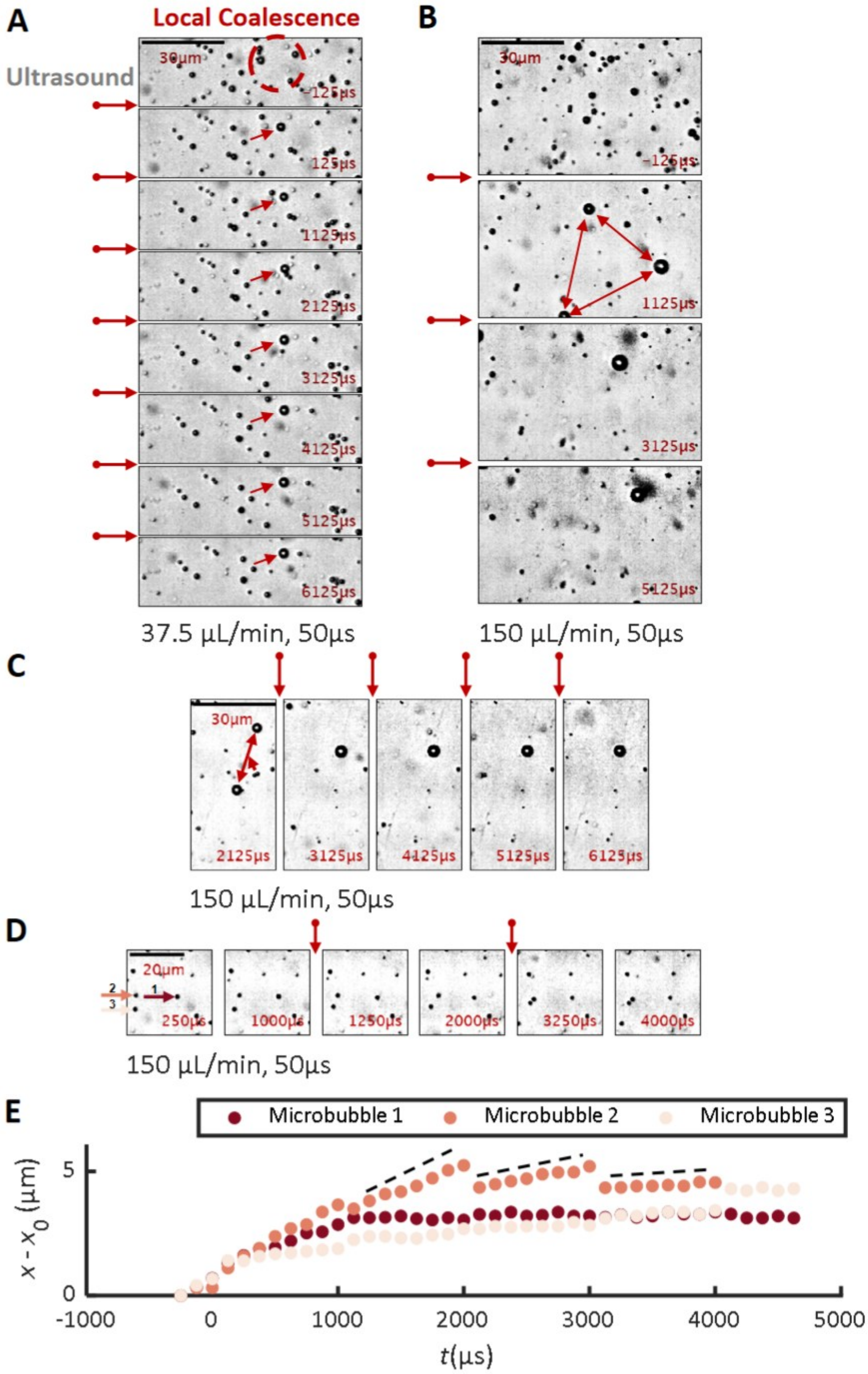

Figure 4. Typical scenarios of microbubble cloud dynamics under multiple short-pulse ultrasound sequences. Selected high-speed snapshots of bubble dynamics under (A) low flow rate (37.5 µl/min) and (B) high flow rate (150 µl/min). The pulse length is 50 µs for all cases shown. Under low flow rate, bubbles within a localized region (red dashed outline) coalesce and form a larger microbubble (radius ≈ 1.7 µm, pointed to by the red arrow). This large microbubble subsequently attracts surrounding microbubbles, which migrate slowly toward it. Under high flow rate, large microbubbles form in multiple regions after the first ultrasound burst and interact with each other over longer distances. After several short-pulse sequences, these bubbles coalesce into a big microbubble (radius ≈ 3.2 µm), effectively clearing

microbubbles from the surrounding area. (C) Coalescence of two large microbubbles and two tiny bubbles under flow rate of 150 µl/min and ultrasound pulse length of 50 µs. After coalescing, the larger microbubble remains stationary at its position and ceases downstream motion. (D) The microbubble dynamics in 'frozen' region. The displacements of three representative microbubbles (indicated by colored arrows) are quantified in (E) using corresponding colors. Bubbles within the 'frozen' region exhibit minimum movement under ultrasound excitation and progressively decreasing downstream velocities. For microbubble 2, the velocity drops markedly between 1000 µs and 3000 µs (dashed line) and it coalesces with microbubble 3 at approximately 4000 µs. After 4000 µs, both bubbles remain stationary.

The typical evolution of bubble dynamics is shown in Fig. 4, where short-pulse ultrasound bursts are emitted every 1 ms (1000 µs). Under low flow rate (Fig. 4A, 37.5 µL/min), only bubbles within a relatively small region (e.g., marked by a red dashed circle with a radius of 10 µm) coalesce after the first ultrasound burst, forming a larger microbubble (radius ≈ 1.7 µm). Subsequently, this larger microbubble gradually attracts surrounding smaller bubbles toward itself after each ultrasound burst. In contrast, under high flow rate (Fig. 4B, 150 µL/min), microbubbles coalesce in multiple regions, leading to the formation of several large microbubbles (average radius ≈ 2.2 µm, at 1125 µs). These larger bubbles interact with each other over longer distances during ultrasound excitation, exhibit pronounced motion, and progressively clearing microbubbles from the surrounding area. Eventually, they merge into a big microbubble (radius ≈ 3.2 µm).

We also observe that microbubbles can become 'frozen' after several ultrasound bursts, both at low flow rate (Fig. 4A, 37.5 µL/min) and at high flow rate (Fig. 4C, 150 µL/min). Both Fig. 4C and Fig. 4A show that, once a large microbubble forms, it remains stationary near its formation point and ceases downstream motion. Such an effect is not unique to large microbubbles but also exist in the 'frozen' zone (Fig. 4D). The trajectories of three representative microbubbles are shown in Fig. 4E, with corresponding-colored arrows labeled in Fig. 4D. Microbubbles within the 'frozen' region exhibit minimum movement under ultrasound excitation and progressively decreasing downstream velocities. Especially for microbubble 2, the velocity drops markedly between 1000 µs and 3000 µs (dashed line) and it coalesces with microbubble 3 at approximately 4000 µs. After 4000 µs, both bubbles remain stationary.

Experimental observations indicate that both low flow rate and repeated short-pulse ultrasound exposure promote the development of "frozen" microbubbles, which remain near their original positions and exhibit minimal displacement during ultrasound excitation. However, longer pulse length do contribute to actively moving microbubbles, and lead to more clustering and coalescence events. This trend is further quantified by measuring the average bubble velocity after each ultrasound burst (Fig. 5). At high flow rate (Fig. 5C, F; 150 µL/min), ultrasound significantly reduces bubble velocity from the 2nd burst ($p < 0.001$), indicating that microbubbles get 'frozen' by short-pulse ultrasound exposure. In contrast, at low flow rate (Fig. 5A, D; 37.5 µL/min), ultrasound has minimal influence on bubble motion, implying that the 'frozen' microbubbles are developed mostly by the low flow rate itself. At intermediate flow rate (Fig. 5B, E; 75 µL/min), a moderate reduction in velocity is observed, particularly under longer pulse duration (100 μs), indicating a combined effect of flow rate and ultrasound exposure. Figure 5G further shows that increasing both pulse length and flow rate leads to a greater reduction in the normalized bubble number, $N_{norm}(t)$.

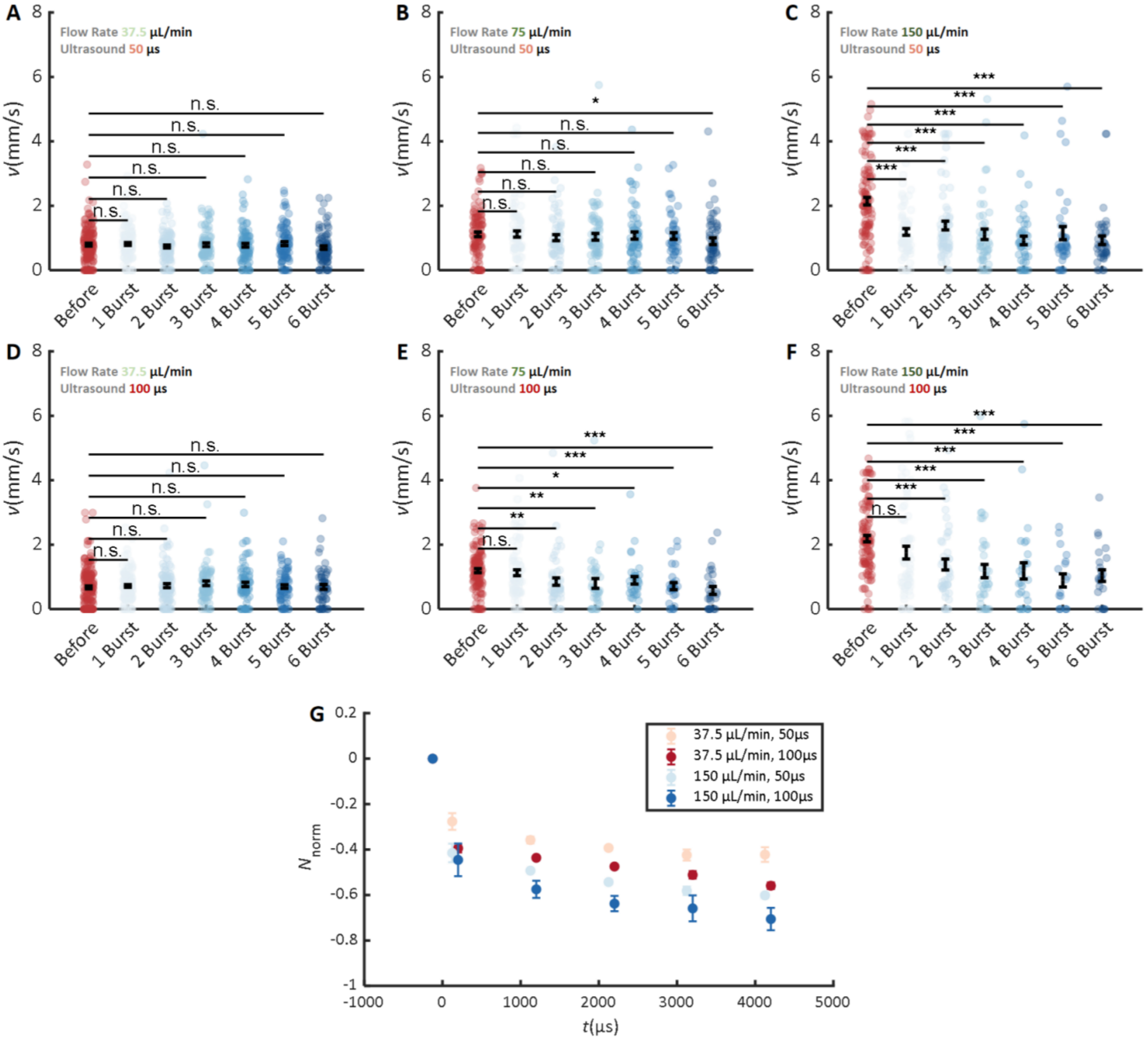

Figure 5. Statistical analysis of microbubble velocity under different conditions. (A) flow rate 37.5 μL/min, pulse length 50 μs; (B) flow rate 75 μL/min, pulse length 50 μs; (C) flow rate 150 μL/min, pulse length 50 μs; (D) flow rate 37.5 μL/min, pulse length 100 μs; (E) flow rate 75 μL/min, pulse length 100 μs; (F) flow rate 150 μL/min, pulse length 100 μs. (G) Microbubble number as a function of time under different conditions. Error bars indicate the standard deviation obtained from independent realizations. Error bars represent Mean ±SEM. Three individual videos are analyzed in each condition.

3.3 Acoustic and hydrodynamic forces exerted on microbubbles

To elucidate the combined effects of short-pulse ultrasound and flow rate on microbubble motion, it is necessary to consider the forces exerted on the microbubbles by both the acoustic excitation and the laminar flow. Prior to ultrasound exposure, microbubbles located near the

PDMS wall within the rectangular microfluidic channel move predominantly in the x-direction, following the Poiseuille flow profile:

$$u_x(z) = (6Qz)/(H^2W) \qquad (1)$$

with a nearly constant shear rate $\gamma = (6Q)/(H^2W)$ [55] nearby the wall, where Q is the volumetric flow rate, H and W are the height and width of the microfluidic channel, respectively, and z denotes the distance from the PDMS wall (with $z = 0$ at the top PDMS wall). In the studied scales [56], the measured microbubble velocity reflects the local Poiseuille flow velocity. Equation (1) therefore indicates that a smaller measured bubble velocity corresponds to a smaller wall distance z.

Prior to ultrasound excitation, microbubbles are transported downstream by laminar flow. Under these conditions, the Saffman force is negligible, and lateral migration is primarily governed by the combined effects of shear-gradient lift and wall-induced lift forces [57]. A simplified expression for the lift force can be written as $F_{lift} = 0.5\rho\gamma(2R)^2$ (ρ is the fluid density, and R is the bubble radius), which is counteracted by buoyancy, F_B [57]. As illustrated in Fig. 6A, at low flow rate (37.5μl/min), buoyancy dominates the lateral motion in the z-direction, driving microbubbles gradually toward the PDMS wall. With increasing flow rate, the lift force becomes stronger and governs the cross-stream migration, resulting in distal motion from the wall under high flow rate conditions (150 μl/min). Consequently, under low flow rate, microbubbles are already positioned close to the PDMS wall prior to ultrasound exposure, and any additional ultrasound-induced motion in the negative z-direction (toward the PDMS wall) is minimal. In contrast, at higher flow rates, the flow-driven migration in the negative z-direction is reduced or reversed, allowing the short-pulse ultrasound excitation to become the dominant factor influencing vertical motion toward the PDMS wall.

To further analyze the influence of ultrasound on microbubble motion in the z-direction, we first consider the time-dependent bubble volume under traveling-wave excitation, which can be described by a Rayleigh–Plesset-type equation [13]

$$\rho\left(\ddot{R}R + \frac{3}{2}\dot{R}^2\right) = \left(P_0 + \frac{2\sigma}{R_0}\right)\left(\frac{R_0}{R}\right)^{3\kappa}\left(1 - \frac{3\kappa\dot{R}}{c}\right) - P_0 - P_A - \frac{2\sigma}{R} - \frac{4\mu\dot{R}}{R} \qquad (2)$$

where ρ is the liquid density, c the speed of sound in the liquid, κ the polytropic exponent of the gas inside the bubble, with P_0 the local hydrodynamic pressure within the channel and P_A the acoustic pressure, μ is the dynamic viscosity. R_0 is the initial bubble radius, R is the time-dependent radius of the bubble and the overdots denote its time derivatives.

The solution of Eq. (2) yields the time-dependent bubble radius, $R(t)$. During ultrasound excitation, the bubble oscillates and experiences an acoustic radiation force arising from the pressure gradient at the bubble location. For a PDMS wall, the acoustic wave emitted by the microbubble and further reflected by the PDMS wall is negligible; therefore, the wall-reflection-induced secondary Bjerknes force can be ignored, and only the primary Bjerknes force is considered. For a traveling ultrasound wave propagating in the positive z-direction, the acoustic pressure field is given by $P_A(z,t) = -p_A \sin(2\pi ft - kz)$, where $k = 2\pi f/c$ is the wavenumber of the wave with frequency $f = 1.125\,\text{MHz}$ and with p_A the acoustic pressure amplitude. The bubble experiences a radiation force $F_{Bjerknes} = -V\nabla P_A$, where both the pressure gradient ∇P_A and the volume V of the bubble are time-dependent with different phase contributions. As a result, the Primary Bjerknes force is unsteady and oscillates in both magnitude and direction. In addition to the acoustic radiation force, the presence of the PDMS wall introduces a hydrodynamic interaction force, F_w, which can be interpreted as the effect of an image microbubble (hydrodynamic mirror). This interaction leads to periodic, unsteady migration of the microbubble toward the wall and can be described using Kelvin impulse theory [58-60].

$$I = \int_0^{T_C} F \, dt \qquad (3)$$

Where the $T_C = 1/f$. Ignoring the surface tension and assuming mild bubble deformation, the wall-induced force F_w can be expressed as $-\rho(4\pi R^2 \dot{R})^2/(16\pi h^2)$ [58-60], where h is the distance between microbubble center and the PDMS wall. Using Eq. (3), we also evaluate the Kelvin impulse contributions from buoyancy and the primary Bjerknes force, and the results are shown in Fig. 6B. The calculations indicate that, during ultrasound excitation, nonlinear bubble oscillations and the resulting hydrodynamic wall-interaction force, F_w, which is significantly larger than the other forces—dominate bubble motion in the z-direction. Consequently, microbubbles tend to migrate toward the PDMS wall during ultrasound exposure. Under high flow rate conditions, the lift force drives bubbles slowly away from the PDMS wall in the absence of ultrasound. However, once short-pulse ultrasound is applied, the strong wall-induced hydrodynamic force rapidly pulls bubbles toward the wall, leading to a pronounced reduction in downstream velocity after a single ultrasound pulse.

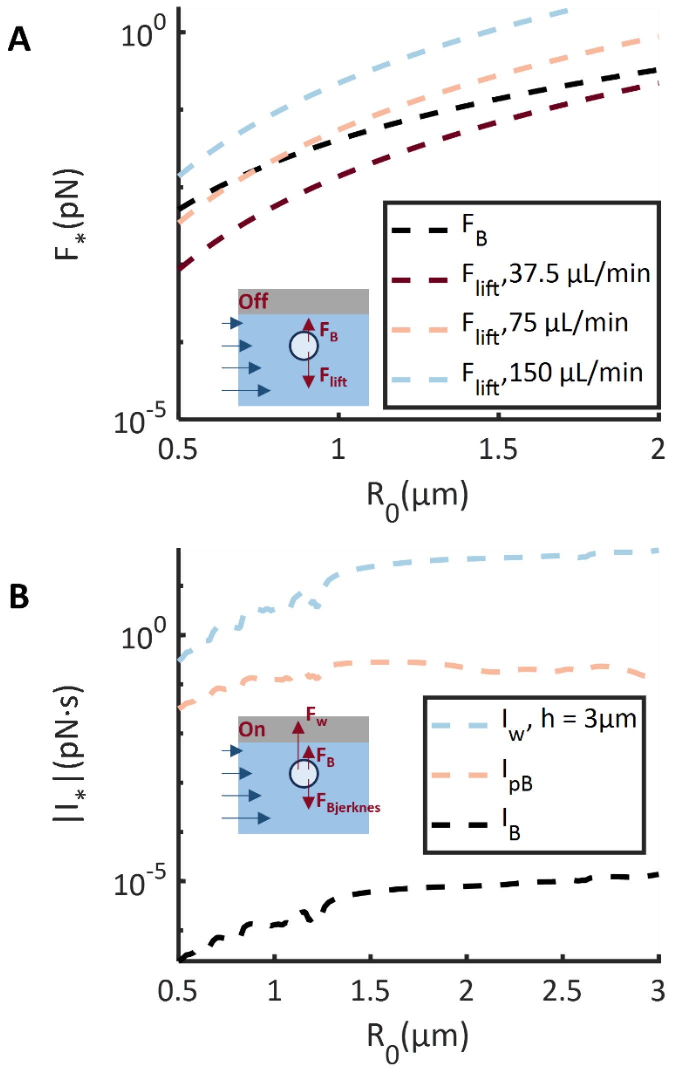

Figure 6. Forces dominate the lateral microbubble motion. (A) The lift force F_{lift} v.s. buoyancy force F_B over different equilibrium bubble radius. (B) The kelvin impulse of F_w, $F_{Bjerknes}$ and F_B (buoyancy force) over different equilibrium bubble radius: I_w v.s. $I_{primary\ Bjerknes}$ and I_B.

The remaining question is why a smaller microbubble–wall distance h promotes the formation of "frozen" microbubbles that exhibit minimal motion under ultrasound excitation. During a short-pulse ultrasound burst, the forces acting on a microbubble can be expressed as follows [61]:

$$0 = F_R + F_A + F_D \qquad (4)$$

where, $F_R = -V\nabla P_R$ denotes the secondary Bjerknes force arising from the acoustic emissions of neighboring microbubbles. This radiation force F_R , attracting in-phase oscillating microbubble moving towards each other, is counteracted by the hydrodynamic drag force near the wall, given by $F_D = \frac{16}{5}\pi\mu U R_0 \ln(\alpha(h - R_0)/R_0)$ [62], where U is the transverse velocity of the microbubble parallel to PDMS wall, and an added mass force $F_A =$

$\frac{1}{2}\rho\frac{d}{dt}(\frac{4\pi}{3}\dot{R}U)$ arises from the acceleration of the surrounding fluid [63]. The coated microbubble can be approximated as a rigid sphere within a point-particle framework. When a smooth particle approaches a wall, lubrication theory predicts a hydrodynamic singularity that prevents the particle from translating at finite forces [64, 65]. A correction factor $\alpha = 10^{-4}$ is used to compensate the underestimate of the idealized model [63-65]. Equation (4) therefore indicates that as the normalized gap $(h - R_0)/R_0$ decreases, the hydrodynamic drag increases, e.g., when h approaches R_0, the drag would become ∞, effectively suppressing bubble motion (with considerably declined U) parallel to the PDMS wall.

Figure 7 presents simulation results based on Eq. (4) for a pair of interacting bubbles near the wall. In Fig. 7A, two representative scenarios illustrate the influence of the wall distance h on lateral bubble motion. For larger h, microbubbles actively migrate toward each other and come into contact within 50 μs, indicating coalescence (case 2). In contrast, for smaller h (case 1), the enhanced wall-induced drag substantially reduces parallel motion, and the bubbles appear effectively "frozen" near their initial positions. The corresponding x–t trajectories (Fig. 7B) show that the normalized gap $(h - R_0)/R_0$,and thus the drag force, is the key parameter determining whether bubbles move actively or become 'frozen' under ultrasound excitation. The regime map in Fig. 7C further demonstrates that as $(h - R_0)/R_0$ decreases, bubble motion becomes increasingly restricted, and the critical bubble separation distance $(d - R_0)/R_0$ required for coalescence is smaller. This means that the closer the bubbles are to the wall, the nearer the two bubbles must be to achieve coalescence.

Based on this force analysis, the combined effects of short-pulse ultrasound and flow rate on microbubble motion can be understood. Under low flow rate, buoyancy dominates over lift forces, driving microbubbles toward the PDMS wall. The relative motion between microbubbles leads to a rapid increase in hydrodynamic drag. As a result, the bubbles become effectively "frozen," and further increases in pulse length have minimal influence on microbubble motion, both parallel and perpendicular to the wall. This is due to the lubrication constraint [66].

With increasing flow rate, the lift force can induce reverse motion in the z-direction, driving microbubbles away from the PDMS wall. However, once short-pulse ultrasound is applied, the wall-induced hydrodynamic force F_w drives the bubbles toward the PDMS wall, thereby reducing the bubble-wall gap thickness. During the first ultrasound burst, microbubbles may therefore remain actively interacting and coalesce into larger bubbles. These larger microbubbles exert stronger secondary Bjerknes forces on one another and can thus remain actively mobile for a longer period. Nevertheless, once a sufficiently thin liquid gap is established, both small microbubbles and isolated large microbubbles become effectively "frozen," exhibiting progressively slower downstream motion and a diminished response to subsequent ultrasound excitation.

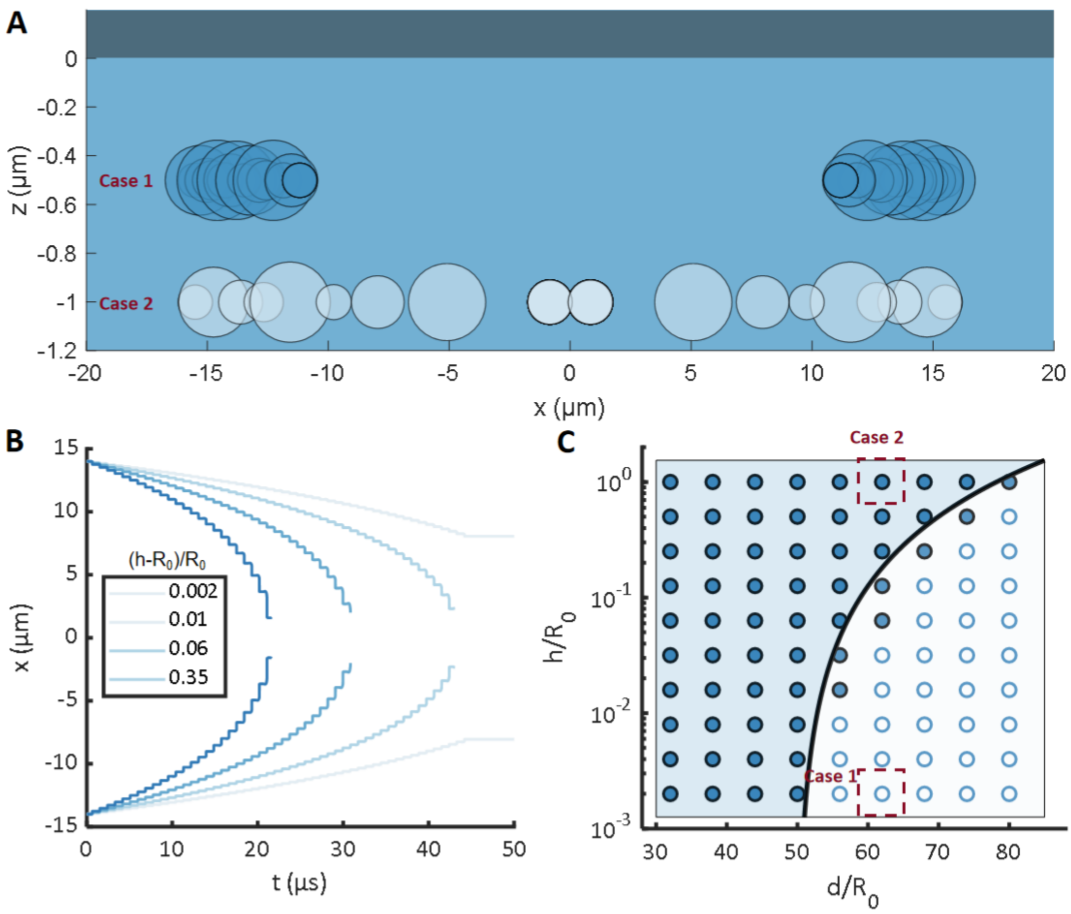

Figure 7. Simulation results of the motion parallel to the wall for a pair of microbubbles with equilibrium radius $R_0 = 0.5$ μm under 50 μs ultrasound exposure. (A) Selected simulation results showing the influence of thin gap water layer $(h - R_0)/R_0$ on the microbubble motion parallel to the wall. (B) Selected x-t diagram of microbubble pair motion. The legend indicates the value of $(h - R_0)/R_0$. (C) Parameter map of $(h - R_0)/R_0$ and $(d - R_0)/R_0$ indicates the regions where the microbubble pair can coalesce with each other. The cases where bubbles can get in touch with each other is considered as a coalescence event (solid dot), and the cases where microbubbles cannot get in touch with each other is considered as non-coalescence events (hollow dot).

4. Discussion

This study demonstrates that microbubble cloud dynamics under short-pulse ultrasound in confined flow are controlled by the dynamic competition between acoustic radiation forces and near-wall hydrodynamic drag. Our high-speed visualizations and quantitative analysis reveal two distinct regimes: an actively interacting regime characterized by clustering and coalescence, and a "frozen" regime in which bubbles exhibit minimal motion under continued acoustic excitation. A theoretical model incorporating lift force, Bjerknes forces, wall-induced hydrodynamic interaction, and hydrodynamic drag with wall correction captures the transition between actively moving and frozen states. The model confirms that both a low flow rate and repeated short-pulse ultrasound sequences promote the development of 'frozen' bubbles near the wall, and that the normalized wall-bubble gap, $(h - R_0)/R_0$, is the critical parameter governing this transition.

The frozen state arises from wall-mediated hydrodynamic drag. During ultrasound excitation, nonlinear bubble oscillations generate a wall-induced interaction force that drives bubbles toward the PDMS boundary. As the bubble–wall gap decreases, lubrication drag increases rapidly and suppresses translational motion parallel to the wall. Once an extremely thin liquid layer forms, further increases in pulse length produce little additional displacement, both parallel and perpendicular to the wall, because lubrication drag dominates over acoustic radiation forces.

Flow rate plays a dual and important role in this process. At low flow rate (37.5 μL/min), buoyancy positions bubbles close to the wall before ultrasound exposure, facilitating rapid establishment of the lubrication-dominated regime. At higher flow rate (150 μL/min), lift forces initially displace bubbles away from the wall, allowing stronger clustering during early bursts. However, repeated short pulses reduce the wall gap and eventually lead to ‘frozen’ bubbles. Pulse length primarily affects the early interaction stage. A longer pulse (100 μs) extends the duration of the attractive secondary Bjerknes force, leading to more pronounced clustering and coalescence within the actively moving region during a single burst. This results in a larger drop in bubble number, consistent with the findings of Zhou et al. (2025) [31], who showed that longer pulse lengths accelerate bubble aggregation. However, once the lubrication constraint is established and bubbles are 'frozen', increases in pulse length have a limited influence on bubble translational motion.

The normalized wall gap $(h - R_0)/R_0$ emerges as the key control parameter governing the transition between ‘actively moving’ and ‘frozen’ states. When this gap is sufficiently large, acoustic radiation forces dominate and promote clustering. When it becomes small, lubrication drag suppresses bubble motion.

Our findings align with and extend those of Zhou et al. (2025) [31] and Memari et al. (2023) [32]. Zhou et al. demonstrated in a flowing phantom that microbubble clustering is the primary cause of temporal non-uniformity in stable cavitation intensity under rapid short-pulse ultrasound. Our study provides a mechanistic explanation by identifying the competition between secondary Bjerknes forces and wall-induced drag as the key physical determinants. We show that clustering is not merely stochastic, but a dynamically controlled process governed by bubble-wall proximity, which is itself modulated by flow rate and ultrasound.

Complementing these insights, Memari et al. [32] reported that faster microbubble flow (30 ml/min) significantly increases endothelial cell membrane permeabilization compared to slower flow (5 ml/min), attributing this to individual bubbles interacting with more cells. Our results offer a bubble-dynamics-centric perspective, revealing an additional layer of complexity: at high flow rates, bubbles initially exhibit greater mobility and active clustering, potentially concentrating mechanical stress. However, they subsequently become 'frozen' near the wall, a state that may produce sustained, localized shear stress on the endothelium, potentially enhancing long-term outcomes through calcium signaling [32, 67, 68].

While our theoretical model captures the key physics governing the transition between bubble states, it is built upon several simplifying assumptions that should be acknowledged. First, the coupling between radial and translational dynamics in our simulation of parallel motion is simplified, even though volume oscillations are accounted for in calculating the wall-induced force via the Kelvin impulse. Second, the model currently considers only pairwise bubble interactions and does not account for the complex, multi-body effects that arise within dense clusters. Third, thermal effects are neglected.

Nevertheless, despite these simplifications, the model successfully reproduces the experimentally observed transition between actively moving and frozen states and identifies the normalized wall gap as the critical control parameter governing this behavior. It is aslo worth noting that in our experimental geometry, the microbubble radius is two orders of magnitude smaller than the channel height (100 μm). This significant size disparity validates several key assumptions in our force analysis. It confirms that the microbubbles act as point particles relative to the scale of the Poiseuille flow profile, allowing us to accurately describe the background flow velocity using Equation (1). This scale separation justifies the use of standard wall-correction models for the hydrodynamic drag force, derived for a sphere near a plane boundary in an otherwise unconfined quiescent or shear flow. The presence of the distant opposite wall (100 μm away) has a negligible effect on the lubrication interaction between a bubble and the nearest (top PDMS) wall.

Our findings provide insights into the design of ultrasound-mediated drug delivery and therapy protocols. First, the existence of a flow-rate-dependent 'frozen' state suggests that therapeutic outcomes will be highly sensitive to the local hemodynamic environment. In slow-flowing tumor vasculature [33, 34], microbubbles may rapidly transition to a 'frozen', wall-adherent state. This could be beneficial for achieving sustained, localized mechanical effects on the endothelium, potentially enhancing extravasation of co-administered drugs. Conversely, in higher-flow healthy vessels, bubbles might remain actively mobile and interact with a larger endothelial surface area, as suggested by Memari et al. [32]. This underscores the need for patient-specific or disease-specific ultrasound protocols that account for variations in blood flow. Second, the 'frozen' state may represent a distinct bioeffect mechanism. An immobilized bubble oscillating persistently against the vessel wall could generate sustained, localized shear stress. This might be more effective at triggering specific cellular responses, such as calcium waves or the activation of mechanosensitive ion channels and signaling pathways [32, 68, 69], compared to a briefly interacting, free-floating bubble. Future studies should correlate the 'frozen' bubble state with specific biological outcomes to determine whether it is a desirable or undesirable state for different therapeutic applications. Third, as our results applies to cases where microbubble size is much smaller compared to the channel height.

In conclusion, the dynamic competition between acoustic radiation forces and near-wall hydrodynamic drag, critically modulated by flow rate and ultrasound pulse sequences, determines the fate of microbubble clouds in confined environments. The transition to a 'frozen' state, governed by the bubble-wall gap, is a key phenomenon to be considered in the rational design of cavitation-based therapies to ensure both efficacy and safety.

CRediT authorship contribution statement

Yi Xu: Investigation, Visualization, Formal analysis, Writing – original draft. **Siyu Luo:** Investigation, Visualization, Formal analysis, Writing – original draft. **Yujie Wang**: Visualization, Formal analysis, Writing – original draft. **Liying Wang:** Visualization, Supervision, Formal analysis, Writing – original draft, Writing – review & editing. **Yuzhe Fan:** Conceptualization, Methodology, Software, Visualization, Supervision, Formal analysis, Writing – original draft, Writing – review & editing. **Fenfang Li:** Conceptualization,

Methodology, Visualization, Supervision, Formal analysis, Writing – original draft, Writing – review & editing, Funding acquisition.

Declaration of Competing Interest

The authors have no conflict of interests to declare.

Data availability

All data supporting the findings of this study are available within the article and its supplementary files. Any additional requests for information can be directed to and will be fulfilled by the corresponding authors.

Acknowledgements

This research was supported by the start-up funding from Shenzhen Bay Laboratory, the Natural Science Foundation of Guangdong Province (Nos. 2023A1515010649), the Guangdong Provincial Pearl River Talents Program 2023QN10X235, the National Natural Science Foundation of China (No. 12204322), and European Regional Development Fund (EFRE)] under grant agreement No. ZS/2024/02/184142.

References

[1] O'reilly M A. Exploiting the mechanical effects of ultrasound for noninvasive therapy[J]. Science, 2024, 385(6714): eadp7206.

[2] Sboros V. Response of contrast agents to ultrasound[J]. Advanced drug delivery reviews, 2008, 60(10): 1117-1136.

[3] Faez T, Emmer M, Kooiman K, et al. 20 years of ultrasound contrast agent modeling[J]. IEEE transactions on ultrasonics, ferroelectrics, and frequency control, 2012, 60(1): 7-20.

[4] Coussios C C, Roy R A. Applications of acoustics and cavitation to noninvasive therapy and drug delivery[J]. Annu Rev Fluid Mech, 2008, 40(1): 395-420.

[5] Cattaneo M, Guerriero G, Shakya G, et al. Cyclic jetting enables microbubble-mediated drug delivery[J]. Nature Physics, 2025, 21(4): 590-598.

[6] Chen H, Kreider W, Brayman A A, et al. Blood vessel deformations on microsecond time scales by ultrasonic cavitation[J]. Physical review letters, 2011, 106(3): 034301.

[7] Fan Y, Ohl C-D. Perforation of thin-membrane-covered soft matter induced by cavitation-initiated extreme mechanics[J]. Physical Review Applied, 2025, 23(2): 024052.

[8] Ohl C-D, Arora M, Ikink R, et al. Sonoporation from jetting cavitation bubbles[J]. Biophysical journal, 2006, 91(11): 4285-4295.

[9] Li F, Yang C, Yuan F, et al. Dynamics and mechanisms of intracellular calcium waves elicited by tandem bubble-induced jetting flow[J]. Proc Natl Acad Sci U S A, 2018, 115(3): E353-e362.

[10] Maeda K, Colonius T. Bubble cloud dynamics in an ultrasound field[J]. Journal of fluid mechanics, 2019, 862: 1105-1134.

[11] Maeda K, Maxwell A D. Controlling the dynamics of cloud cavitation bubbles through acoustic feedback[J]. Physical Review Applied, 2021, 15(3): 034033.

[12] Fan Y, Li H, Zhu J, et al. A simple model of bubble cluster dynamics in an acoustic field[J]. Ultrasonics Sonochemistry, 2020, 64: 104790.

[13] Fan Y, Li H, Fuster D. Time-delayed interactions on acoustically driven bubbly screens[J]. The Journal of the Acoustical Society of America, 2021, 150(6): 4219-4231.

[14] Mettin R, Akhatov I, Parlitz U, et al. Bjerknes forces between small cavitation bubbles in a strong acoustic field[J]. Physical review E, 1997, 56(3): 2924.

[15] Louisnard O. A simple model of ultrasound propagation in a cavitating liquid. Part II: Primary Bjerknes force and bubble structures[J]. Ultrasonics sonochemistry, 2012, 19(1): 66-76.

[16] Lanoy M, Derec C, Tourin A, et al. Manipulating bubbles with secondary Bjerknes forces[J]. Applied Physics Letters, 2015, 107(21).

[17] Gumerov N A, Akhatov I S. Modes of self-organization of diluted bubbly liquids in acoustic fields: One-dimensional theory[J]. The Journal of the Acoustical Society of America, 2017, 141(2): 1190-1202.

[18] Fan Y, Li H, Xu C, et al. Influence of bubble distributions on the propagation of linear waves in polydisperse bubbly liquids[J]. The Journal of the Acoustical Society of America, 2019, 145(1): 16-25.

[19] Postema M, Marmottant P, Lancée C T, et al. Ultrasound-induced microbubble coalescence[J]. Ultrasound in medicine & biology, 2004, 30(10): 1337-1344.

[20] Rychak J J, Klibanov A L, Hossack J A. Acoustic radiation force enhances targeted delivery of ultrasound contrast microbubbles: in vitro verification[J]. IEEE transactions on ultrasonics, ferroelectrics, and frequency control, 2005, 52(3): 421-433.

[21] Rychak J J, Klibanov A L, Ley K F, et al. Enhanced targeting of ultrasound contrast agents using acoustic radiation force[J]. Ultrasound in medicine & biology, 2007, 33(7): 1132-1139.

[22] Kovacs Z I, Kim S, Jikaria N, et al. Disrupting the blood–brain barrier by focused ultrasound induces sterile inflammation[J]. Proceedings of the National Academy of Sciences, 2017, 114(1): E75-E84.

[23] Shin J, Kong C, Cho J S, et al. Focused ultrasound–mediated noninvasive blood-brain barrier modulation: preclinical examination of efficacy and safety in various sonication parameters[J]. Neurosurgical Focus, 2018, 44(2): E15.

[24] Pouliopoulos A N, Kwon N, Jensen G, et al. Safety evaluation of a clinical focused ultrasound system for neuronavigation guided blood-brain barrier opening in non-human primates[J]. Scientific reports, 2021, 11(1): 15043.

[25] Jordão J F, Thévenot E, Markham-Coultes K, et al. Amyloid-β plaque reduction, endogenous antibody delivery and glial activation by brain-targeted, transcranial focused ultrasound[J]. Experimental neurology, 2013, 248: 16-29.

[26] Choi J J, Selert K, Vlachos F, et al. Noninvasive and localized neuronal delivery using short ultrasonic pulses and microbubbles[J]. Proceedings of the National Academy of Sciences, 2011, 108(40): 16539-16544.

[27] Lim Kee Chang W, Chan T G, Raguseo F, et al. Rapid short-pulses of focused ultrasound and microbubbles deliver a range of agent sizes to the brain[J]. Scientific Reports, 2023, 13(1): 6963.

[28] Morse S V, Mishra A, Chan T G, et al. Liposome delivery to the brain with rapid short-pulses of focused ultrasound and microbubbles[J]. Journal of Controlled Release, 2022, 341: 605-615.

[29] Morse S V, Pouliopoulos A N, Chan T G, et al. Rapid short-pulse ultrasound delivers drugs uniformly across the murine blood-brain barrier with negligible disruption[J]. Radiology, 2019, 291(2): 459-466.

[30] O'reilly M A, Waspe A C, Ganguly M, et al. Focused-ultrasound disruption of the blood-brain barrier using closely-timed short pulses: influence of sonication parameters and injection rate[J]. Ultrasound Med Biol, 2011, 37(4): 587-594.

[31] Zhou Q, Tan C, Liu C, et al. Regulating microbubble clusters for improving temporal uniformity of stable cavitation intensity under rapid short-pulse ultrasound[J]. Ultrasonics Sonochemistry, 2025: 107582.

[32] Memari E, Hui F, Yusefi H, et al. Fluid flow influences ultrasound-assisted endothelial membrane permeabilization and calcium flux[J]. J Control Release, 2023, 358: 333-344.

[33] Jain R K. Determinants of tumor blood flow: a review[J]. Cancer Res, 1988, 48(10): 2641-2658.

[34] Yuan F, Leunig M, Huang S K, et al. Microvascular permeability and interstitial penetration of sterically stabilized (stealth) liposomes in a human tumor xenograft[J]. Cancer Res, 1994, 54(13): 3352-3356.

[35] Scremin O U, Li M G, Scremin A M, et al. Cholinesterase inhibition improves blood flow in the ischemic cerebral cortex[J]. Brain Res Bull, 1997, 42(1): 59-70.

[36] Li C, Ma Y, Liu M, et al. Characteristics of flow fields in the gas–liquid mini-bubble columns with particle image velocimetry measurements[J]. AIChE Journal, 2022, 68(9): e17798.

[37] Sennoga C A, Seddon J M, Frueh J A, et al. Dynamics of targeted microbubble adhesion under pulsatile compared with steady flow[J]. Ultrasound in Medicine & Biology, 2014, 40(10): 2445-2457.

[38] Yan F, Li X, Jiang C, et al. A novel microfluidic chip for assessing dynamic adhesion behavior of cell-targeting microbubbles[J]. Ultrasound in Medicine & Biology, 2014, 40(1): 148-157.

[39] Acconcia C N, Leung B Y, Winch G, et al. Acoustic radiation force induced accumulation and dynamics of microbubbles on compliant surfaces[J]. Physics in Medicine & Biology, 2019, 64(13): 135003.

[40] Juang E K, De Cock I, Keravnou C, et al. Engineered 3D microvascular networks for the study of ultrasound-microbubble-mediated drug delivery[J]. Langmuir, 2018, 35(31): 10128-10138.

[41] Pouliopoulos A N, Li C, Tinguely M, et al. Rapid short-pulse sequences enhance the spatiotemporal uniformity of acoustically driven microbubble activity during flow conditions[J]. The Journal of the Acoustical Society of America, 2016, 140(4): 2469-2480.

[42] De Maio A, Lin F-H, Stefanovic B, et al. Tissue-type Differences in Focused Ultrasound and Microbubble-mediated Drug Delivery to the Brain Exist at Vessel Level[J]. Theranostics, 2026, 16(4): 1975.

[43] Zhang X, Huk D, Wang Q, et al. A microfluidic shear device that accommodates parallel high and low stress zones within the same culturing chamber[J]. Biomicrofluidics, 2014, 8(5).

[44] Park W, Choi M J, Lee J S, et al. Embedded 3D-Coaxial Bioprinting of Stenotic Brain Vessels with a Mechanically Enhanced Extracellular Matrix Bioink for Investigating Hemodynamic Force-Induced Endothelial Responses[J]. Advanced Functional Materials, 2025, 35(50): e04276.

[45] Juste-Lanas Y, Hervas-Raluy S, García-Aznar J M, et al. Fluid flow to mimic organ function in 3D in vitro models[J]. APL bioengineering, 2023, 7(3).

[46] Li S, Liu X, Zhang L, et al. Integrated applications of microfluidics, organoids, and 3D bioprinting in in vitro 3D biomimetic models[J]. International Journal of Bioprinting, 2025, 11(3): 115-153.

[47] Cai Y, Fan K, Lin J, et al. Advances in BBB on chip and application for studying reversible opening of blood–brain barrier by sonoporation[J]. Micromachines, 2022, 14(1): 112.

[48] Li F, Yuan F, Sankin G, et al. A Microfluidic System with Surface Patterning for Investigating Cavitation Bubble(s)-Cell Interaction and the Resultant Bioeffects at the Single-cell Level[J]. J Vis Exp, 2017, (119).

[49] Squires T M, Quake S R. Microfluidics: Fluid physics at the nanoliter scale[J]. Reviews of modern physics, 2005, 77(3): 977-1026.

[50] Van Der Kroon I, Quinto-Su P A, Li F, et al. Acoustically driven cavitation cluster collapse in planar geometry[J]. Phys Rev E Stat Nonlin Soft Matter Phys, 2010, 82(6 Pt 2): 066311.

[51] Helfield B, Chen X, Watkins S C, et al. Biophysical insight into mechanisms of sonoporation[J]. Proceedings of the National Academy of Sciences, 2016, 113(36): 9983-9988.

[52] Qiao C, Luo S, Liu Z, et al. Tuning Endothelial Barrier Permeability with Ultrasound: A Pulse-Length-Dependent Interplay Between Bubble Dynamics and Cellular Bioeffects[J]. LangTaoSha Preprint Server,

2026.

[53] Shen Y, Cai Y, Qiao C, et al. A bottom-up approach to understanding ultrasound mediated blood–brain barrier opening using long and short pulses[J]. bioRxiv, 2025: 2025.2006.2011.659100.

[54] Heiles B, Chavignon A, Hingot V, et al. Performance benchmarking of microbubble-localization algorithms for ultrasound localization microscopy[J]. Nature Biomedical Engineering, 2022, 6(5): 605-616.

[55] Bruus H. Theoretical microfluidics[M]. Oxford university press, 2007.

[56] Poelma C. Ultrasound imaging velocimetry: a review[J]. Experiments in Fluids, 2017, 58(1): 3.

[57] Zhang J, Yan S, Yuan D, et al. Fundamentals and applications of inertial microfluidics: a review[J]. Lab on a Chip, 2016, 16(1): 10-34.

[58] Blake J R. The Kelvin impulse: application to cavitation bubble dynamics[J]. The ANZIAM Journal, 1988, 30(2): 127-146.

[59] Xu P, Li B, Ren Z, et al. Dynamics of a laser-induced buoyant bubble near a vertical rigid boundary[J]. Physical Review Fluids, 2023, 8(8): 083601.

[60] Supponen O, Obreschkow D, Tinguely M, et al. Scaling laws for jets of single cavitation bubbles[J]. Journal of Fluid Mechanics, 2016, 802: 263-293.

[61] Segers T, Versluis M. Acoustic bubble sorting for ultrasound contrast agent enrichment[J]. Lab on a Chip, 2014, 14(10): 1705-1714.

[62] Goldmans A, Brenner H. Slow viscous motion of a sphere parallel to a plane wall-I Motion through a quiescent fluid[J]. Chemical Engineering Science, 1967, 22: 637651.

[63] Watanabe T, Kukita Y. Translational and radial motions of a bubble in an acoustic standing wave field[J]. Physics of Fluids A: Fluid Dynamics, 1993, 5(11): 2682-2688.

[64] Zeng L, Najjar F, Balachandar S, et al. Forces on a finite-sized particle located close to a wall in a linear shear flow[J]. Physics of fluids, 2009, 21(3).

[65] Nanayakkara S, Zhao J, Terrington S, et al. Effects of surface roughness on the drag coefficient of spheres freely rolling on an inclined plane[J]. Journal of Fluid Mechanics, 2024, 984: A13.

[66] Zhou Z, Jin G, Tian B, et al. Hydrodynamic force and torque models for a particle moving near a wall at finite particle Reynolds numbers[J]. International Journal of Multiphase Flow, 2017, 92: 1-19.

[67] Li F, Yang C, Yuan F, et al. Dynamics and mechanisms of intracellular calcium waves elicited by tandem bubble-induced jetting flow[J]. Proceedings of the National Academy of Sciences, 2018, 115(3): E353-E362.

[68] Lin J, Qiao C, Jiang H, et al. Reversible Ca2+ signaling and enhanced paracellular transport in endothelial monolayer induced by acoustic bubbles and targeted microbeads[J]. Ultrasonics Sonochemistry, 2025, 112: 107181.

[69] Li F, Park T H, Sankin G, et al. Mechanically induced integrin ligation mediates intracellular calcium signaling with single pulsating cavitation bubbles[J]. Theranostics, 2021, 11(12): 6090.